Frontiers in Mechanochemistry and Mechanical Alloying

INCOME2008
1-4 December, 2008

THE MICROSTRUCTURE, TEXTURE AND MECHANICAL PROPERTIES OF AS-ECAE INTERSTITIAL-FREE STEEL AND COPPER

Azdiar A. Gazder[1ξ], Florian H. Dalla Torre[2], Christopher H.J. Davies[3], Elena V. Pereloma[1]
[1]School of Mechanical Materials & Mechatronics Engineering, University of Wollongong, NSW 2522, Australia
[2]Laboratory of Metal Physics and Technology, ETH Zurich, Wolfgang-Pauli-Str. 10, 8093, Zurich, Switzerland
[3]Department of Materials Engineering, Monash University, VIC 3800, Australia

Keywords: Equal Channel Angular Extrusion (ECAE); Equal Channel Angular Pressing (ECAP); Transmission Electron Microscopy (TEM); Electron Back-Scattering Diffraction (EBSD); Texture

Abstract

A comparison between the microstructure, texture and mechanical properties of bcc interstitial-free (IF) steel and fcc copper (Cu) for up to N = 8 passes Equal Channel Angular Extrusion (ECAE) via route B_C processing was undertaken. Transmission Electron Microscopy (TEM) and Electron Back-Scattering Diffraction (EBSD) studies revealed that the deformation microstructures of both metals evolves from low-angled microbands and dislocation cells after N=2 passes towards more equiaxed, homogeneous subgrain/grain structures comprising higher-angles of misorientation after N = 8 passes. In both metals, the percentage rise in Σ3 and random boundaries are attributed to mechanisms that favour low-energy boundary configurations during ECAE. Texture evolution involves gradual changes in individual component strengths during multi-pass ECAE. The bcc and fcc textures are correlated by interchanging the Miller indices of the slip plane and slip direction between the two cubic crystal systems. The uniaxial tensile curves of both materials are representative of significant cold-working and depict higher 0.2% proof stresses, a small period of uniform elongation, necking and lastly, failure via geometrical softening. Constitutive modelling suggests that rather than a change in deformation mechanism, the preservation of ductility up to N = 8 passes is associated with an increase in the mean free path of dislocations; with slip via dislocation glide remaining as the dominant carrier of plastic strain in both metals.

Introduction

Severe plastic deformation (SPD) techniques such as Equal Channel Angular Extrusion (ECAE) have elicited significant interest over the last decade as methods that are capable of producing fully dense and bulk ultrafine grained (UFG) materials with high mechanical strengths. In this context, Cu remains the best-studied material to-date ([1-3] and the references therein) and has only recently been outnumbered by publications on steels [1-7]. The latter is due to the burgeoning demand for the higher strength and more affordable steels in Asia.

Despite the availability of scientific literature on both these materials on an individual basis, very few studies have compared them together on the basis of their morphology and behaviour in the as-deformed state. Recently, we performed a TEM-based microstructure and bulk texture investigation on IF-steel and Cu subjected to route B_C processing for up to N = 4 passes [8]. Therein the Taylor factors of prominent crystallographic orientations were estimated under conditions of uniaxial tension via the least work criterion [9]. The work presented here updates the above comparison with even newer insights into the deformation behaviours of the two materials for up to N = 8 passes. It focuses on correlating the as-deformed TEM and EBSD statistics and bulk texture data to their overall effect on mechanical properties during uniaxial tension. Emphasis has been placed on subgrain/grain sizes, misorientation distributions and special boundary relationships. The texture work highlights the interchangeability of crystallographic plane and direction when tabulating the ideal simple shear orientations of the two crystal systems. Moreover, the similarities in texture evolution due to the employed processing route are also detailed.

The uniaxial tensile properties characterise the changes in strength, total elongation to failure and the normalised work hardening rate with increasing pass number. The uniform plastic region is simulated using the Kocks-Mecking-Estrin (KME) single parabola, total dislocation density approach for Stage-III work hardening [10]. Specific to the above, it is noted that as-SPD materials are also known to display Stages- IV and V work hardening. In such cases, the constitutive modelling of mechanical data is undertaken via a "composite" approach that accounts for dislocation density evolution in the cell walls and interiors [11]. However, previous compression tests on Cu have shown that Stages IV (up to N = 4 passes) and V (N ≥ 4 passes) work hardening are reached beyond uniform strains of ~5% [12]. Consequently, the necking of dog-boned samples occurs at far earlier strains during tension than the barrelling of cylindrical samples during compression; a Stage-III only the work hardening model is still applicable during room temperature, uniaxial tensile testing of UFG materials in the as-deformed state.

Experimental Procedure

Commercial-grade IF-steel plate (Fe–0.003C–0.15Mn–0.03Al–0.08Ti–0.007Si–0.01P–0.005S–0.001N, wt.%) from BlueScope Steel Limited and Oxygen-Free High Conductivity (OFHC) Cu bars (99.98 wt.% purity) were machined into 20 × 20 × 80 mm^3 billets, annealed at 973K for 1 hour (IF-steel) and 873K for 2 hours (Cu) and allowed to furnace cool. The grain size distribution in the annealed materials was measured using optical microscopy and fitted by a log-normal distribution. The mean

ξ email : azdiar@uow.edu.au

grain size was 140 ± 10 μm for IF-steel and 11 ± 4 μm for copper. The annealed billets were subjected to room temperature ECAE for up to N = 1, 2, 4 and 8 passes via route B_C processing using a Φ = 90°, Ψ = 0° die-set at 5 $mm.s^{-1}$ (IF-steel) and 3 $mm.s^{-1}$ (Cu) with 25 MPa back-pressure.

For TEM, EBSD and bulk texture analysis, only *x* (or ED) -plane specimens cut from the center of the stable billet length were used (Fig. 1). TEM was conducted on a Phillips CM-20 at 200 kV after electrolytically thinning the foils on a Struers Tenupol-5 electropolisher with a solution of 5% perchloric acid and 95% methanol (IF-steel) or 25% orthophosphoric acid, 25% ethanol, 50% distilled water (Cu). Polishing conditions were maintained at 50 V, 300 mA at −30 °C for IF-steel and 10 V, 150 mA at 20 °C for Cu. Bright-field (BF) images and selected area diffraction (SAD) patterns with aperture diameters of 5.4 μm (complete BF area) and 1.1 μm (representative of the centre of an area of interest) were taken along the ⟨111⟩ and ⟨110⟩ zone axes of IF-steel and Cu, respectively.

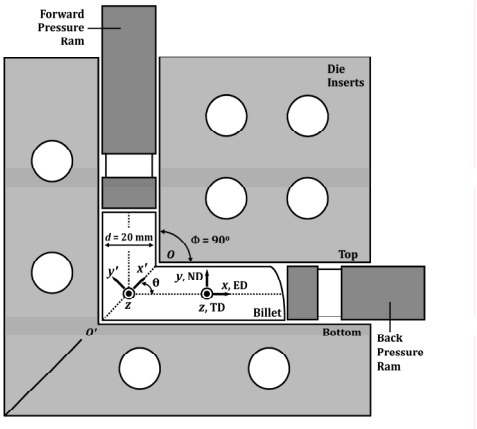

Figure 1. Schematic of the ECAE die-set with a half-way extruded billet indicating the adopted coordinate system for Φ = 90° ECAE. *(Not to scale)*. Reproduced from Gazder *et al.* [70] copyright 2006, with permission from Elsevier

Each EBSD specimen was ground and polished to 1 μm surface finish followed by light etching using OP-S Silica solution. The EBSD maps were obtained on a LEO-1530 Field Emission Gun – Scanning Electron Microscope (FEG-SEM) fitted with a Nordlys-II™ EBSD detector operating at 20 kV and ×15k (IF-steel) and ×20k (Cu) magnification. Two orientation image maps of 15 × 20 μm^2 (IF-steel) and 10 × 18 μm^2 (Cu) were scanned from the centre of the *x*-plane of each sample using a step size of 80 nm (IF-steel) and 40 nm (Cu).

Texture analysis was performed on a GBC-MMA texture goniometer equipped with a Cu-K_α anode (wavelength λ = 1.54 Å) and a polycapillary beam enhancer resulting in a collimated beam of 10 × 10 mm^2. The IF-steel {110}, {200}, {211}, and Cu {111}, {200}, {220} incomplete pole figures (χ = 0°– 80°) were used to calculate the orientation distribution functions (*f(g)*) using the spherical harmonics method without imposing sample symmetry conditions. $g = (\phi_1, \Phi, \phi_2)$ refers to grain orientations denoted by the three Euler angles in Bunge's notation [13]. All textures were rotated to the TD-view and will be discussed in the *xyz* laboratory reference coordinate system (Fig. 1) [14, 15].

In order to characterise the mechanical properties, similarly processed as-ECAE billets were machined into round tensile samples of ø4 mm diameter with 15 mm (IF-steel) and 25 mm (Cu) gauge length. Room temperature uniaxial tensile testing was undertaken on a screw-driven Instron 4505 operating at initial strain rates of 0.83 × 10^{-3} s^{-1} (IF-steel) and 1.67 × 10^{-3} s^{-1} (Cu). Using a purpose-written tolerance-divergence MATLAB® subroutine, an optimised elastic modulus was estimated by comparing a bulk texture – based modelled modulus [16] with experimental tensile test data for each as-ECAE condition. Following this, the 0.2% ($\sigma_{0.2}$) proof stress, the ultimate tensile strength (σ_{UTS}) and the uniform and total elongations were calculated.

Results and Discussion

Evolution of Deformation Microstructure

Micrographs of N = 1 pass IF-steel and Cu (Fig. 2(a) and 3(a)) record the formation of a microstructures comprising high dislocation density substructures along with extended and parallel (sub)grain boundaries. The microbands typically consist of long, thin plate-like features that are confined to single grains with sharp boundaries (and visible thickness fringes) oriented parallel to the ⟨110⟩ (IF-steel) and ⟨111⟩ (Cu) directions. The traces indicate the operation of the {110}⟨111⟩ and {111}⟨110⟩ slip systems of bcc and fcc materials, respectively.

The interior of these banded substructures consist of dislocation cells of one to four elements arranged either normal or inclined to the boundary width. While the cell walls are diffused (clearly distinguishable by the locally higher dislocation density, and dislocation debris characterised by fuzzy diffraction contrasts) and consist of tangled arrays of dislocations, the dislocation density between these walls is low.

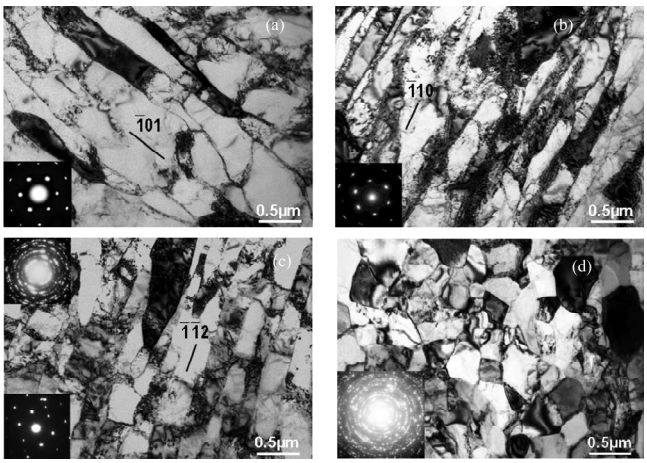

Figure 2. Bright-field TEM micrographs and SAD patterns of IF-steel from the *x* (or ED) -plane after (a) N = 1 pass, (b) N = 2, (c) N = 4 and (d) N = 8 passes. SAD representative of the entire micrograph are bottom inserts in (a), (b), (d) and top insert in (c). (a-c) Reproduced from Li *et al.* [15] copyright 2006, with permission from Elsevier.

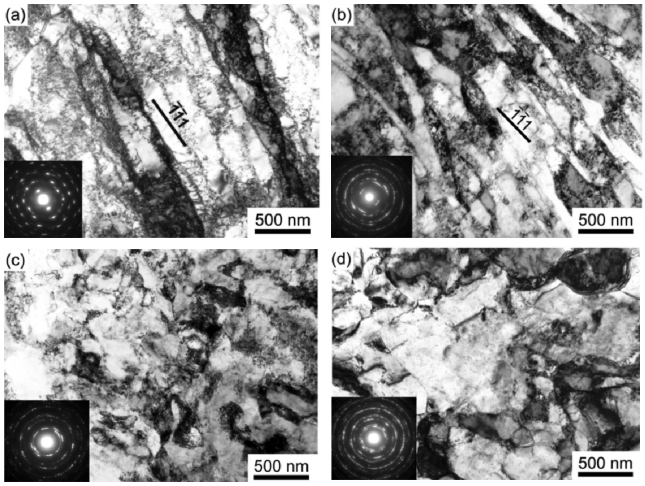

Figure 3. Bright-field TEM micrographs and SAD patterns of Cu from the *x* (or ED) -plane after (a) N = 1 pass, (b) N = 2, (c) N = 4 and (d) N = 8 passes. (a)-(d) Reproduced from Dalla Torre *et al.* [30] copyright 2006, with permission from Springer.

After N = 2 passes (Fig. 2(b) and 3(b)), strongly elongated and substantially thinner microbands are typically observed in both materials. The operation of additional slip systems with lamellar boundaries oriented along the trace of the {112} (IF-steel) and {220} (Cu) planes were also locally observed. Although most microbands still exhibit low-angled character (≤15° misorientation), the SAD patterns after the second pass suggest a slight increase in the average misorientation angles of both materials compared to the N = 1 pass condition.

After N = 4 passes (Fig. 2(c) and 3(c)), the substructure of both metals comprises strongly elongated lamellae which coexists with an even larger area fraction of nearly-equiaxed subgrains having more clearly defined boundaries. The misorientation angle is higher in areas where equiaxed grains are more dominant as compared to regions where lamellar boundaries remain persistent. Concurrent with previous reports [7, 17], the SAD confirms the trend of an increase in average misorientation with greater strain as a result of the continuous transformation of former cells into subgrains.

By N = 8 passes (Fig. 2(d) and 3(d)), the fraction of strongly elongated microbands is noticeably reduced in both metals as most areas are characterised by approximately equiaxed subgrains with high angles of misorientation between their boundaries. The intense straining per pass coupled with ever higher accumulated strains results in the truncation of prior elongated boundaries and leads to greater subgrain/grain refinement.

Qualitatively speaking, evolution of the deformation microstructure is similar in both, IF-steel and Cu. As suggested in [18-20], subgrain walls formed by the re-arrangement of trapped glide dislocations during one pass act as further barriers to dislocation propagation during a successive pass. Consequently, the various HAGBs select different combinations of slip systems to accommodate the next increment of strain during multiple passes [21]. As deformation proceeds, each substructure rotates to the nearest stable end-orientation and results in both, the generation of new boundaries and a further rotation of pre-existing boundaries to even higher angles of misorientation [20].

It is understood that larger area fractions of high-angled boundaries form via increased magnitudes of dislocation storage at the cell/subgrain boundaries [22]. But at the same time, boundary dislocation density for highly strained materials is characterised by an upper limit and shares an inverse relationship with the square of the dislocation spacing [23]. Thus, increasing the level of imparted strain enhances the likelihood of activation of mechanical annihilation processes (involving *in-situ* local recovery effects [23]) and results in even larger boundary misorientation angles [24, 25].

The statistics returned from TEM and EBSD (Table 1 and 2) show that microstructural evolution can be separated into two distinct accumulated strain intervals. The first accumulated strain interval extends up to N = 4 passes and is characterised by rapid subgrain/grain refinement and significant reductions in the area fraction of low-angled boundaries (Table 2). In the second accumulated strain interval between N = 4 and 8 passes, an attenuation of the measures of microstructural evolution occurs as a marked decrease in the rate of subgrain/grain refinement is seen in both materials. Most importantly, throughout this second strain interval, the average grain size remains roughly equivalent as it approaches the subgrain diameter (Table 1 and 2).

If IF-steel and Cu are compared on a per-pass basis, distinct variations in the rates of substructure evolution (for example - the achieved subgrain/grain morphology, boundary area fractions, average misorientation and distribution profile and special boundary relationships) are noted.

In agreement with earlier TEM-based studies on bcc and fcc materials [15, 26], N = 4 and 8 passes IF-steel retains a greater area fraction of elongated substructures compared to Cu. The remanent microbands at N = 8 passes are different from those after N = 4 passes as they are no longer straight but comprise a wavy contrast (or corrugation [27]), have greatly reduced average lengths and widths and show incomplete glide reversal despite multiple passes [15, 28]. Bulk textures after N = 4 and 8 passes also substantiate the last observation as Cu records distinct cube orientation components similar to its N = 0 pass condition whereas the corresponding initial orientations of as-ECAE IF-steel remain extremely weak.

In agreement with [29], EBSD maps of N = 8 passes Cu notes the presence of some large (up to 0.5 μm) grains characterised by sharp and straight boundaries which could be precursors to recrystallised grains [30]. (i) An enhancement of grain structures showing sharp boundaries and low dislocation density interiors, (ii) the presence of stacking fault tetrahedra, dislocation loops and few lattice dislocations in the large grains after N = 8 passes and, (iii) an overall decrease in the total dislocation density (calculated via the Taylor equation) from 2.7×10^{15} m^{-2} to 1.2×10^{15} between N = 2 and 8 passes correlates well with higher levels of dislocation annihilation at subgrain/grain boundaries due to the increasing boundary misorientation and the operation of recovery/ reorganisation -type processes (*see* [30] for further details).

Table 1. TEM measured changes in the average spacing between subgrain boundaries (ASSB) and the average dislocation cell widths (ADCW) for IF-steel and Cu after N = 1, 2, 4 and 8 passes

TEM		IF-steel				Cu			
		1	2	4	8	1	2	4	8
ASSB	(μm)	0.37	0.34	0.23	0.21	0.22	0.21	0.17	0.18
ADCW	(μm)	0.10	0.12	0.08	0.09	-na-	-na-	-na-	-na-

Table 2. EBSD measured changes in average percentage area fraction (A_F), misorientation (θ), coincidence-site-lattice (CSL) and random boundaries, equivalent circle diameter (d_{ECD}), linear intercept (L) and aspect ratio (λ) for IF-steel and Cu after N = 1, 2, 4 and 8 passes

EBSD			IF-steel				Cu			
			1	2	4	8	1	2	4	8
A_F	(%)	LAGBs	94.1	89.8	62.2	46.3	65.1	-na-	47.6	37.6
		MAGBs	4.1	6.3	18.2	16.7	18.0	-na-	18.4	18.3
		MHAGBs	1.3	2.6	12.4	14.7	7.0	-na-	15.9	20.8
		VHAGBs	0.4	1.3	7.2	22.3	9.9	-na-	18.1	23.4
		HAGBs	5.9	10.2	37.8	53.7	34.9	-na-	52.4	62.5
θ	(°)	AVG	6.2	7.4	16.6	24.5	16.4	-na-	23.3	27.4
		LAGBs	4.8	4.8	6.2	6.6	6.6	-na-	6.6	6.3
		MAGBs	21.0	21.4	23.0	23.3	22.4	-na-	23.6	24.0
		MHAGBs	36.2	38.9	38.8	39.5	38.9	-na-	39.8	39.6
		VHAGBs	53.5	51.7	51.6	52.9	54.2	-na-	52.5	52.9
		HAGBs	27.4	29.4	33.7	40.1	34.8	-na-	38.5	40.0
Σ3	(%)	AVG	0.1	0.1	0.4	1.8	3.4	-na-	1.8	3.8
		HAGBs	0.5	0.8	0.9	3.2	8.7	-na-	3.2	5.7
Σ5-29b	(%)	AVG	1.0	0.9	2.6	3.5	1.7	-na-	4.0	3.9
		HAGBs	14.0	7.3	5.9	6.0	4.3	-na-	7.1	5.8
Random	(%)	AVG	4.9	9.1	34.8	48.4	29.8	-na-	26.9	21.6
		HAGBs	85.5	91.8	93.2	90.8	87.0	-na-	89.7	88.5
Skewness			2.4	2.6	2.0	1.4	2.1	-na-	2.2	2.5
Kurtosis			5.0	5.9	3.7	1.6	2.4	-na-	6.1	10.1
d_{ECD}	(μm)	AVG	0.49	0.37	0.30	0.28	0.54	-na-	0.41	0.31
L	(μm)	AVG	0.51	0.37	0.29	0.27	0.18	-na-	0.22	0.14
λ		AVG	1.88	1.75	1.65	1.71	2.33	-na-	1.87	1.77

In as-ECAE IF-steel (Table 2), the misorientation profile is biased towards higher class intervals (skewness) but the relative rate of flattening of the misorientation distribution (kurtosis) occurs faster than the corresponding increase in the relative frequency of misorientation to higher class intervals [31-33]. The opposite trend is observed in the misorientation distribution of Cu. Here the slight shift towards lower class intervals and marked "peakedness" of the misorientation profile that continues up to N = 8 passes evidences a far greater rate of substructure reorganisation than IF-steel during multi-pass ECAE.

Both metals depict a reduction in the percentage of Σ1 (or LAGBs) boundaries and a proliferation of higher numerical index and more mobile Σ5-29b boundaries with increasing number of passes [34]. In most cases, the percentage of Σ3 or Σ5-29b boundaries associated with the HAGBs are approximately double those compared to the total boundary population. Concurrently, boundary fractions that do not satisfy the Brandon criterion are designated as "random" grain assemblies. The random fraction is found to increase slightly in IF-steel but remains approximately constant in Cu with higher pass number.

The ~2 to 4% of Σ3 boundaries after every pass suggests the possibility of twinning during ECAE [22]. This is surprising since deformation twinning is not energetically favourable at low strain rates and room temperature due to the many slip systems still able to operate in bcc and fcc metals.

In the bcc case, the twinning domain decreases with smaller grain size and significant plastic strain. Conversely, severely deformed bcc materials are known to be more prone to ⟨111⟩ -axis pseudo-symmetry errors occurring at ~30° and 60° misorientation. This results in Σ3 boundary fractions that include remnants/artefacts from statistical mis-indexing or orientations

close to Σ3 boundaries rather than denoting twin formation. As a further note, even a mathematically generated random distribution of grains contains some Σ3 boundaries. To this end, the values in Table 2 are within range of the Σ3 (1.6%) and random boundary (89%) populations of a Mackenzie distribution comprising only grain boundaries [45]. Thus, in light of the above evidence obtained to-date, this study discounts twinning in as-ECAE IF-steel.

In heavily deformed Cu via ECAE or HPT, several studies have shown the presence of coherent twins and stacking faults [27, 35-37]. Twinning in fcc materials is said to be more feasible after substantial strain hardening occurs or when a critical dislocation density is reached or occurs in areas of high strain localisation (such as in or at shear bands) [38, 39]. Although the driving force for twin nucleation in Cu has been modelled by a reduction in the total dislocation density [40] unambiguous delineation of the twin nucleation mode (i.e. - whether the twins are deformation induced or are created by processes similar to those operating during annealing) has not been possible to-date.

In the present study on Cu, Σ3 boundaries were mainly restricted to areas of shear banding after N = 1 pass but become widely distributed beyond N = 4 passes. Although the constitutive modelling of as-ECAE Cu records an overall reduction in dislocation density between N = 4 and 8 passes (Table 4), a concurrent decrease in mechanical strength is also noted. Moreover, extensive TEM investigations on the same material [27, 30, 41] have also failed to indicate unambiguous twin morphologies. Rather, TEM revealed dislocations moving towards boundaries and forming ledges (most probably due to stress incompatibility) [27,41,42]. Ordinarily, these ledges are associated with stacking faults and a high density of grain boundary dislocations. But on the other hand, the ledges could also resemble those typically related to the initiation of annealing twins (as suggested by the 'pop-out' mechanism) and where growth occurs via the migration of the incoherent and more mobile Σ3 boundaries [40]. Thus, our work shows that Σ3 boundaries can have different geometries and comprise, apart from symmetric tilt boundaries (or coherent twin boundaries), incoherent twins ($\Sigma 3^{n}$) and stacking faults [43, 44].

Specific to the EBSD maps shown in Fig. 4, it is understood that microstructural features smaller than 80 nm (IF-steel) and 40 nm (Cu) step size cannot be delineated. Despite this apparent imitation in the EBSD map statistics, the presence of a significant area fraction of Σ3 boundaries and random grain assemblies can also be correlated with the operation of recovery/reordering mechanisms during ECAE. The latter tend to favour low-energy boundary configurations [41, 42].

Bulk Crystallographic Texture

The as-annealed N = 0 textures of IF-steel and Cu are very weak. In IF-steel it is featured by {001}⟨110⟩ and {110}⟨001⟩ components in the rolling convention (Fig. 5(a)). In Cu, the texture consists of a ⟨111⟩+⟨001⟩ duplex fiber with the fiber axis parallel to the billet longitudinal axis (Fig. 5(b)).

For bcc and fcc metals, the location of the ideal orientations and partial fibers that comprise the ideal negative simple shear components after N = 1 pass Φ = 90° ECAE are illustrated in the key pole figures projected onto the TD-plane (Fig. 6). Thus the N = 1 pass pole figures consist of orientations that distribute themselves along two partial fibers running along: (i) {110} (IF-steel) or {111} (Cu) planes with ⟨*uvw*⟩ directions CCW-rotated by θ = 45° around the TD from the ND-plane and, (ii) [*hkl*] planes with ⟨111⟩ (IF-steel) or ⟨110⟩ (Cu) directions CCW-rotated by θ = 45° around the TD from the ED.

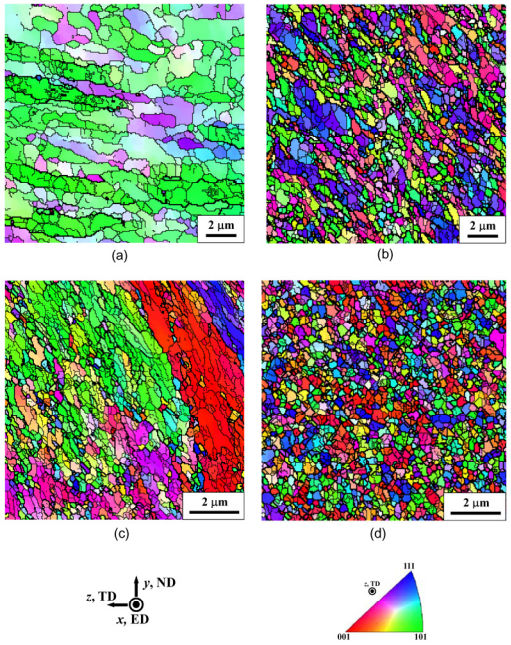

Figure 4. Representative inverse pole figure maps of (a), (b) IF-steel and (c), (d) Cu from the *x* (or ED) -plane after (a), (c) N = 1 pass and, (b), (d) N = 8 passes

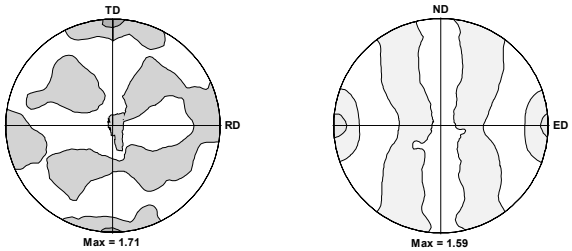

Figure 5. Experimental (110) and (111) pole figures of the initial N = 0 texture of (a) IF-steel and (b) Cu. In the case of IF-steel plate, TD and RD indicate the transverse and rolling directions of the billet in the rolling convention and are parallel to the ND and ED of the ECAE rig die-set, when the billet is inserted in the inlet channel. For Cu, the longitudinal axis of the billet is horizontal to the rod. *Contour levels: 0.5*×

In order to differentiate between the two materials in the present work, the partial fibers are abbreviated using the subscript θ for IF-steel and the italicised subscript θ for Cu. They are thus re-designated as: $\{110\}\langle uvw\rangle_{\theta}$ (or $\{110\}_{\theta}$) and $\{hkl\}\langle 111\rangle_{\theta}$ (or $\langle 111\rangle_{\theta}$) –type partials for IF-steel. In the case of Cu, they are referred to as $\{110\}\langle uvw\rangle_{\theta}$ (or $\{110\}_{\theta}$) and $\{hkl\}\langle 110\rangle_{\theta}$ (or $\langle 110\rangle_{\theta}$) –type partials.

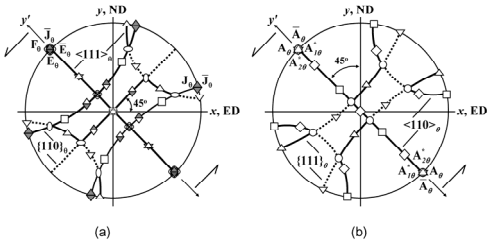

Figure 6. Key (110) end texture pole figures depicting simple shear orientations and partial fibers (solid lines) for (a) bcc [28] and (b) fcc materials [14, 50] after N = 1 pass at Φ = 90° ECAE. Refer to Table 3 for legend. Reproduced from (a) Li *et al* [15] and (b) Gazder *et a.* [70] copyright 2006, with permission from Elsevier

Table 3. Ideal crystallographic orientations and texture fibers for bcc [15, 28] and fcc [14] materials after N = 1 pass

bcc Notation		Equivalent TD-rotation by θ = 45°	Fiber Family
$D_{1\theta}$	▽	$(\bar{1}\ \bar{1}\ 2)[1\ 1\ 1]_\theta$	$\langle 1\ 1\ 1\rangle_\theta$
$D_{2\theta}$	△	$(1\ 1\ \bar{2})[1\ 1\ 1]_\theta$	$\langle 1\ 1\ 1\rangle_\theta$
E_θ	⬭	$(1\ 1\ 0)[1\ \bar{1}\ 1]_\theta$	$\langle 1\ 1\ 1\rangle_\theta$, $\{1\ 1\ 0\}_\theta$
$\bar{E}_\theta$	0	$(\bar{1}\ \bar{1}\ 0)[\bar{1}\ 1\ \bar{1}]_\theta$	$\langle 1\ 1\ 1\rangle_\theta$, $\{1\ 1\ 0\}_\theta$
J_θ	◈	$(1\ 1\ 0)[1\ \bar{1}\ 2]_\theta$	$\{1\ 1\ 0\}_\theta$
$\bar{J}_\theta$	◈	$(\bar{1}\ \bar{1}\ 0)[\bar{1}\ 1\ \bar{2}]_\theta$	$\{1\ 1\ 0\}_\theta$
F_θ	□	$(1\ 1\ 0)\langle 0\ 0\ 1\rangle_\theta$	$\{1\ 1\ 0\}_\theta$
fcc Notation		Equivalent TD-rotation by $\theta = 45°$	Fiber Family
$A^*_{1\theta}$	△	$(1\ 1\ 1)[\bar{1}\ \bar{1}\ 2]_\theta$	$\{1\ 1\ 1\}_\theta$
$A^*_{2\theta}$	▽	$(1\ 1\ 1)[1\ 1\ \bar{2}]_\theta$	$\{1\ 1\ 1\}_\theta$
A_θ	○	$(1\ \bar{1}\ 1)[1\ 1\ 0]_\theta$	$\{1\ 1\ 1\}_\theta$, $\langle 1\ 1\ 0\rangle_\theta$
$\bar{A}_\theta$	○	$(\bar{1}\ 1\ \bar{1})[\bar{1}\ \bar{1}\ 0]_\theta$	$\{1\ 1\ 1\}_\theta$, $\langle 1\ 1\ 0\rangle_\theta$
B_θ	◇	$(1\ \bar{1}\ 2)[1\ 1\ 0]_\theta$	$\langle 1\ 1\ 0\rangle_\theta$
$\bar{B}_\theta$	◇	$(\bar{1}\ 1\ 2)[\bar{1}\ \bar{1}\ 0]_\theta$	$\langle 1\ 1\ 0\rangle_\theta$
C_θ	□	$(0\ 0\ 1)\langle 1\ 1\ 0\rangle_\theta$	$\langle 1\ 1\ 0\rangle_\theta$

Similar to the ideal simple shear case, the {110} and {111} N = 1 pass experimental pole figure for IF-steel and Cu contain dyadic symmetry and an inversion center projected on to the *z*-plane. In the case of IF-steel, it consists of a partial $\{110\}_\theta$ fiber running from F_θ to E_θ / $\bar{E}_\theta$ ('/' symbolises 'or') through J_θ / $\bar{J}_\theta$ orientations and a partial $\langle 110\rangle_\theta$ fiber extending from $D_{1\theta}$ to $D_{2\theta}$ through E_θ / $\bar{E}_\theta$. Relatively higher orientation densities can be found near the F_θ and $D_{1\theta}$ components. It was shown in [28] that the $D_{1\theta}$ (or near $D_{1\theta}$) component is stronger than the $D_{2\theta}$ component as a result of negative simple shear. This is attributed to the fact that the $D_{1\theta}$ orientation is present on both, the $\langle 111\rangle_\theta$ and $\{112\}\langle uvw\rangle_\theta$ (or $\{112\}_\theta$) fibers.

In Cu the pole figure consists of a partial $\langle 110\rangle_\theta$ fiber running from C_θ to A_θ / $\bar{A}_\theta$ through B_θ / $\bar{B}_\theta$ orientations and a partial $\{110\}_\theta$ fiber extending from $A^*_{1\theta}$ to $A^*_{2\theta}$ through A_θ / $\bar{A}_\theta$. Relatively high orientation densities can be found near the C_θ and $A^*_{1\theta}$ components. Analogous to the bcc case, a recent study [46] showed that the $A^*_{1\theta}$ (or near $A^*_{1\theta}$) component is stronger than the $A^*_{2\theta}$ component as a result of *negative* simple shear.

Multiple N ≥ 2 passes results in a gradual texture evolution with the loss of monoclinic sample symmetry characterised by a distinct non-uniformity and incompleteness in orientation density amongst the various fibers. This is ascribed to the +/- 90° rotation about the billet longitudinal axis such that the *z*-axis is no longer a dyad axis when the billet is loaded for successive passes. Bulk textures as a result of Route B_C processing tend to develop slightly stronger $D_{1\theta}$ (in IF-steel) and $A^*_{1\theta}$ (in Cu) orientations and substantially weaker $D_{2\theta}$, F_θ (IF-steel) and $A^*_{2\theta}$, C_θ (Cu) components in comparison to other ideal orientations and can be correlated with the strain level texture changes seen in earlier torsion experiments [47-49].

In agreement with [50] and the present TEM results, both materials show the weak re-appearance of some texture components belonging to the initial N = 0 pass condition after every four passes that reflect incomplete glide-reversal effects that return only part of the substructure into equiaxed configuration. The slight shift of orientation components away from their ideal positions with greater pass number is attributed to the absence of stable orientations after shear-type deformation [47,50]. Moreover, the density spread of individual orientation components with increasing pass number also results in an overall decrease in maximum texture intensity *f(g)*.

Studies on fcc materials have anticipated a change in deformation mechanism (slip giving way to grain rotation and slide) if preceded by small grain sizes and a trend towards randomisation of the overall crystallographic texture [51, 52]. However, the present results show that the as-ECAE texture components remain reasonably approximated by ideal simple shear orientations along their respective partial fibers in both materials; without any large-scale tendencies towards random orientation distributions. In agreement with the TEM and EBSD statistics, the rough constancy in texture components also suggests a plateau in substructure refinement after multiple passes and the predominant operation of dislocation mediated slip.

The textures clearly indicate that the development of $\{110\}_\theta$ and $\langle 111\rangle_\theta$ partial fibers via $\{110\}+\{112\}\langle 111\rangle$ slip in bcc IF-steel and $\{111\}_\theta$, $\langle 111\rangle_\theta$ partial fibers associated with $\{111\}\langle 111\rangle$ slip in fcc Cu. This implies a well-preserved correlation of as-ECAE textures between bcc and fcc materials; intrinsically resulting from the interchangeability of the slip plane and slip direction between the two cubic crystal structures. The

interchangeability is valid not only for N = 1 pass but also holds for multiple passes. Alternatively, Cu shows a primary texture component between $\overset{*}{A}_{1\theta}$ ($(111)[\bar{1}\bar{1}2]_\theta$) and $\bar{A}_\theta$ ($(\bar{1}1\bar{1})[\bar{1}\bar{1}0]_\theta$); with a tendency of orientation flow from $\bar{A}_\theta$ *to* $\overset{*}{A}_{1\theta}$ with increasing pass number. The $D_{1\theta}$ and $\bar{E}_\theta$ orientations in bcc metals correspond to $A_{1\theta}$ and $\bar{A}_\theta$ orientations in fcc metals by exchanging the *hkl*'s and *uvw*'s of their Miller indices. In both materials, this effect of texture component rotation becomes more readily apparent with increasing pass number (Fig. 7).

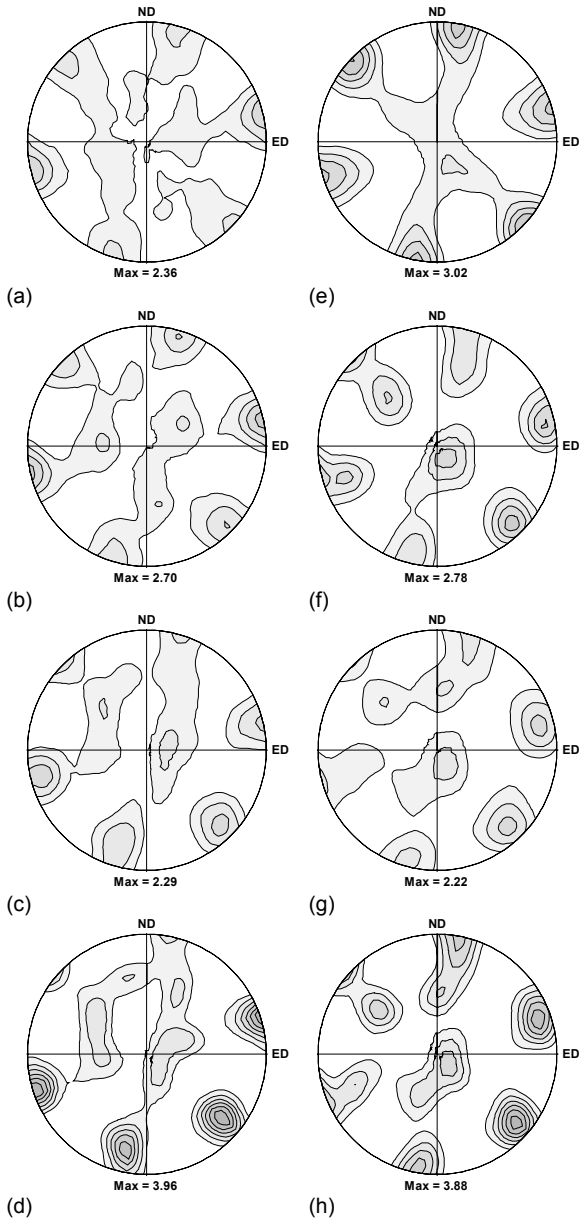

Figure 7. Experimental (110) and (111) *end*-texture pole figures of (a)-(d) IF-steel and (e)-(h) Cu after: (a), (e) N = 1 pass; (b), (f) N = 2 passes; (c), (g) N = 4 passes; and, (d), (h) N = 8 passes. Contour *levels: 0.5*×.

Mechanical Properties and Constitutive Modelling

At N = 0 passes, both materials exhibit continuous yielding, a large region of work hardening and a relatively low yield ratio ($\sigma_{0.2}/\sigma_{UTS}$) (Fig. 8(a),(c)). The extensive period of work hardening is attributed to the mean free dislocation length being comparable to the annealed grain size and the relative ease of mobility of the so-generated dislocations.

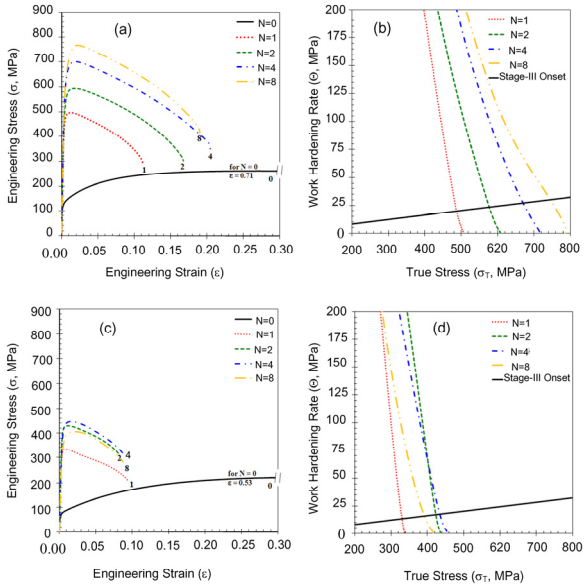

Figure 8. (a), (c) Engineering stress (σ) versus strain (ε) and (b), (d) work hardening rate (Θ) versus true stress (σ_T) curves of (a), (b) IF-steel and (c), (d) Cu after N = 0, 1, 2, 4 and 8 passes

After N = 1 pass the tensile curves are typical of substantially cold-worked materials. They are characterised by a sharp increase in true $\sigma_{0.2}$ and σ_{UTS} -values, a more than doubling of the yield ratio and a large reduction in total elongation (Table 4). A small amount of strain hardening occurs upon yielding as $\varepsilon_{0.2}$ -values increase almost two-fold and ε_{UTS} reduces by approximately twenty times in both materials. The above mechanical behaviour corresponds well with a deformation substructure comprising: (i) a high density of dislocation introduced via shear deformation and, (ii) the smallest substructure size starting to approach that of the dislocation mean free length. The mechanical properties after N = 2 and 4 passes agree with the trends shown in the published literature [53, 54] such that only slight increases in $\sigma_{0.2}$ and σ_{UTS} – values and an approximate plateau in yield ratios is noted.

In both as-ECAE materials, the hardening period is followed almost immediately by necking and an extended region of geometrical softening [55]. The small region of uniform plastic strain is bounded by approximately constant $\varepsilon_{0.2}$ and $\varepsilon_{Neck} = \varepsilon_{UTS}$ values for IF-steel but slightly increasing ε_{UTS} -values for Cu (Table 4).

Table 4. Changes in average mechanical strength ($\sigma_{0.2}$ and σ_{UTS}), yield ratio, total elongation, estimated Taylor factor (M), Stage-III saturation shear stress (τ_{III}^{s}), dislocation storage (K_1) and annihilation (K_2), total dislocation density at 0.2% proof stress ($\rho_{0.2}$) and ultimate tensile strength (ρ_{UTS}) for IF-steel and Cu after N = 1, 2, 4 and 8

Mechanical Properties		IF-steel					Cu				
		0	1	2	4	8	0	1	2	4	8
$\sigma_{0.2}$	(MPa)	126.3	475.6	549.2	640.1	691.5	72.5	325.4	420.5	413.1	341.6
$\varepsilon_{0.2}$		0.0026	0.0045	0.0050	0.0060	0.0062	0.0027	0.0049	0.0058	0.0058	0.0050
σ_{UTS}	(MPa)	263.9	499.4	591.8	702.3	780.6	223.6	333.9	430.7	447.2	404.9
ε_{UTS}		0.2710	0.0123	0.0164	0.0196	0.0195	0.3546	0.0094	0.0119	0.0167	0.0247
$\sigma_{0.2}/\sigma_{UTS}$		0.48	0.95	0.93	0.91	0.89	0.32	0.97	0.98	0.92	0.84
ε_{Total}		71.3	11.1	16.6	20.2	19.0	52.9	9.4	8.2	8.8	8.7
M		3.06	3.07	3.08	3.08	3.08	2.31	2.32	2.31	2.31	2.32
τ_{III}^{s}	(MPa)	118.5	166.2	195.2	232.3	260.3	145.5	148.3	188.9	196.9	178.4
K_1	($x10^9 m^{-2}$)	0.2	11.7	11.5	15.4	11.1	0.2	23.0	23.2	19.2	10.9
K_2		6.8	310.8	252.9	230.2	171.2	5.5	566.1	435.0	342.6	266.7
$\rho_{0.2}$	($x10^{15} m^{-2}$)	0.1	1.3	1.7	2.5	3.0	0.1	1.6	2.7	2.6	1.2
ρ_{UTS}	($x10^{15} m^{-2}$)	0.6	1.4	2.1	3.1	3.9	1.3	1.7	2.8	3.1	1.7

Theoretically, the onset of necking occurs when material strength by work hardening is greater than its load-bearing ability. But in as-SPD materials, the start of necking is exacerbated by an accelerated and localised decrease in cross-sectional area due to variations in the length-scales of the as-deformed substructures and the existence, propagation and concentration of regions of shear banding [56]. The instability criterion predicts the necking point as a function of dislocation activity which in turn, increases the defect population and the flow stress from the yield point to the maximum tensile stress. Thus, as the work hardening approaches zero (in late Stage-III), geometrical softening by lattice reorientations result in shear banding [55-58]. While the shear bands tend to reduce dislocation density and leave behind defect-free channels that permit easier glide [58], but their propagation and proliferation also causes strain localisation within the bands. This strain concentration produces even further plastic instabilities and the entire process accelerates recursively until failure.

Interestingly, the average value of total engineering strain to failure irrespective of the number of passes remains constant in both materials (averaging 16.7% and 8.8% for IF-steel and Cu, respectively between N = 1 and 8 passes (Table 4)). Keeping this in mind, it should be remembered that crystallographic studies had concluded that while all as-deformed textures are ideally representative of negative simple shear, the strength of individual orientation components were processing route-specific [15]. However, strain localisation effects negate the possibility of inducing ductility along more preferred orientations in the as-deformed state. Thus, texture-related heterogeneities tend not to affect the uniform plastic strain in the as-ECAE condition. It is therefore more useful to ascertain the mechanisms that preserve ductility in the as-deformed state after ECAE.

In this context, a roughly constant Taylor factor and the continued proliferation of a dislocation cell-based microstructure [59] suggest that the driving force for re-organisation during multi-pass ECAE is accompanied by a decrease in the overall elastic energy of the dislocations [60,61]. TEM results indicate that the dislocation cell size (and correspondingly the mean free path of dislocations) remains roughly constant beyond N = 1 pass [15] and could correspond to a decrease in the micro-strain during multi-pass ECAE. On the other hand, the increasing area fraction of HAGBs (which are known to be effective sinks for incoming lattice dislocations) after every pass can also reduce the sources of plastic instability and thus, further preserve the region of uniform plastic elongation.

With specific regard to as-ECAE Cu, the uniform and total elongations are not just maintained (as seen in the case of IF-steel) but increase slightly with greater pass number. Concurrently, strain rate jump tests in compression mode have indicated that although the strain rate sensitivity in as-ECAE Cu is higher than its coarse-grained counterpart, the value is still not high enough to prevent the onset of early necking [62].

The above anomaly is better understood when the slight gains in ductility are correlated with the substantial decrease in strength (compare N = 4 passes with N = 8 passes in Table 4 and Fig. 8(c)) and the normalised work hardening rate such that :

$$\Theta = \left(1/\sigma_T\right)\cdot\left(\partial\sigma_T/\partial\varepsilon_T\right)_{\dot{\varepsilon}}$$

Since smaller decreases in the work hardening rate are noted with increasing pass number (Fig. 8d)), it can be surmised that the microstructure regains the ability to work harden, store additional dislocations and consequently, accommodate greater plastic deformation. These observations can in turn, be linked

back to microstructure recovery/reordering processes that reduce the total dislocation density and the volume fraction of cells/boundaries and increase the mean free path of dislocations [27]. Again, such processes could be triggered by the ongoing transformation of non-equilibrium boundaries (such as cell walls with low misorientation angles between them) to more equilibrium boundaries with higher misorientation angles.

The present results show the applicability of the "single parabola" glide-based modelling approach to as-ECAE single-phase IF-steel and Cu for Stage-III deformation. While all tensile samples have undergone a change in strain path from negative simple shear to uniaxial tension, this change is neglected while explaining the hardening response in the context of classical strain-hardening theory.

In Stage-II work hardening, the inhomogeneous dislocation networks are transferred into cell walls and produce the homogeneous cell structures associated with Stage-III deformation via extensive dislocation storage [63]. The onset of Stage-III work hardening occurs when the continuous decrease in work hardening with increasing stress is concurrent with the operation of a dislocation annihilation component. As a result, the approximately parabolic Stage-III work hardening curve depicts a decreasing hardening rate when compared to the linear Stage-II work hardening and can be associated with the processes of dynamic annihilation [64-67]. The absence of a geometry factor in the model (accounting for the re-organisation of the deformation cell structures) prevents the use of the term "dynamic recovery".

It should be noted that a rough constancy in the density of geometrically necessary dislocations is obtained between N = 1 and 8 passes for both metals as it is calculated using $K=1/(bd)$; where b is the Burgers vector and d signifies the roughly constant smallest microstructural feature. However, since both TEM [15] and EBSD [59] show scale-related variations in microstructural features, it is unlikely that the density of the geometrically necessary dislocations is constant throughout: (i) the tensile volume at the beginning of the test or, (ii) the region of uniform plastic strain during uniaxial tension.

In Table 4, K_1 is the athermal dislocation storage component (in m^{-1}) while K_2 is a unit-less quantity denoting dislocation annihilation. The two mechanisms are on different scales with dislocation storage being several orders of magnitude higher than dislocation annihilation. In agreement with Fang *et al.* [68, 69], K_1 and K_2 record decreasing values with increasing pass number as the stress-induced change in dislocation free path (and not the relatively small dislocation annihilation rate) is responsible for the decrease of strain hardening rate and the occurrence of Stage-IV deformation. It is speculated that the increasing HAGB area fraction also changes the rate of dislocation annihilation; especially more so when Stage-III deformation is operative only at boundary areas. However, the lack of substructure geometry factors does not allow for these changes to be quantitatively assessed. Overall though, since the fitting is based on the evolution of the smallest microstructural feature (in this case, the average dislocation cell width), constancies in the various dislocation contributions can be considered as reasonable approximations.

Conclusions

The microstructures, bulk textures and mechanical properties of bcc IF-steel and fcc Cu subjected to ECAE for up to N = 8 passes via route B_C processing has been compared using TEM, EBSD, XRD, uniaxial tensile testing and constitutive modelling via the single parabola approach.

While both materials record variations in the rate of individual microstructural parameters, substructure evolution under as-ECAE conditions can be separated into two distinct strain intervals involving: (i) grain size refinement until it approaches the subgrain size and, (ii) a concurrent increase in misorientation accumulation at the boundaries. Assessment of the grain boundary character distribution suggests that the Σ3 and random boundary populations can be correlated with recovery/reordering rather than twinning for up to N = 8 passes.

Irrespective of the material and the pass number, an approximately constant region of uniform plasticity is followed by necking and an extended region of geometrical softening; resulting in failure via strain localisation. Along with the persistence of a LAGB network, the re-occurrence of Stage-III work hardening occurs continuously for up to N = 8 passes and corresponds to a length scale of the same order as that deduced from dislocation spacings in the cell wall boundaries. Constitutive modelling suggests that the deformation kinetics for up to N = 8 passes are dictated by the interaction of lattice dislocations in both metals.

References

1. H.-K. Kim, M.-I. Choi, C.-S. Chung, D.H. Shin, *Mat. Sci. Eng. A,* 340 (2003) 243.
2. H.S. Kim, W.S. Ryu, M. Janecek, S.C. Baik, Y. Estrin, *Adv. Eng. Mat.,* 7 (2005) 43.
3. J. Kim, I. Kim, D.K. Shin, *Scr. Mater.* 45 (2001) 421.
4. K.-T. Park, Y.-S. Kim, J.G. Lee, D.H. Shin, *Mat. Sci. Eng. A,* 293 (2000) 165.
5. B. Peeters, M. Seefeldt, C. Teodosiu, S.R. Kalidindi, P. Van Houtte, E. Aernoudt, *Acta Mater.,* 49 (2001) 1607.
6. D.H. Shin, B. C. Kim, Y.S. Kim, K.-T. Park, *Acta Mater.,* 48 (2000) 2247.
7. D.H. Shin, I. Kim, J. Kim, K.-T. Park, *Acta Mater.* 49 (2001) 1285.
8. A.A. Gazder, F. Dalla Torre, C.F. Gu, C.H.J. Davies, E.V. Pereloma, *Mat. Sci. Eng., A* 415 (2006) 126.
9. W.F. Hosford, *The Mechanics of Crystals and Textured Polycrystals*, Oxford University Press, New York (1993).
10. Y. Estrin, *J. Mat. Pro. Tech.,* 80-81 (1988) 33.
11. Y. Estrin, L.S. Tóth, A. Molinari, Y. Bréchet, *Acta Mater.,* 46 (1998) 5509.
12. R. Lapovok, F.H. Dalla Torre, J. Sandlin, C.H.J. Davies, E.V. Pereloma, P.F. Thomson, Y. Estrin, *J. Mech. Phys. Sol.,* 53 (2005) 729.
13. H.-J. Bunge, *Texture Analysis in Materials Science: Mathematical Methods*, Butterworth & Co., Berlin (1982).
14. S. Li, I.J. Beyerlein, C.T. Necker, D.J. Alexander, M.A. Bourke, *Acta Mater.,* 52 (2004) 4859.
15. S. Li, A.A. Gazder, I.J. Beyerlein, C.H.J. Davies, E.V. Pereloma, *Acta Mater.,* 54 (2006) 1087.

16. G.E. Deiter, *Mechanical Metallurgy*, McGraw-Hill Book Company, Singapore (1988).
17. Y. Fukuda, K. Oh-ishi, Z. Horita, T.G. Langdon, *Acta Mater.,* 50 (2002) 1359.
18. M.A. Meyers, V.F. Nesterenko, J.C. LaSalvia, Q. Xue, *Mat. Sci. Eng. A,* 317 (2001) 204.
19. A. Mishra, V. Richard, F. Grégori, R.J. Asaro, M.A. Meyers, *Mat. Sci. Eng. A*,410-411 (2005) 290.
20. P.B. Prangnell, J.R. Bowen, A. Gholinia, *Proceedings of the 22nd Risø International Symposium on Materials Science: Science of Metastable and Nanocrystalline Alloys - Structure, Properties and Modelling*, Denmark (2001), p. 105.
21. P.L. Sun, P.W. Kao, C.P. Chang, *Scr. Mater.,* 51 (2004) 565.
22. Yu.V. Ivanisenko, R. Z. Valiev, H.-J. Fecht, *Mat., Sci. Eng. A* 390 (2005) 159.
23. J.D. Embury, *Mat. Sci. Eng., A* 175 (1994) 105.
24. R.Z. Valiev, Yu.V. Ivanisenko, E.F. Rauch, B. Baudelet, *Acta Mater.,* 44 (1996) 4705.
25. A.P. Zhilyaev, B.-K. Kim, G.V. Nurislamova, M.D. Baró, J.A. Szpunar, T.G. Langdon, *Scr. Mater.,* 46 (2002) 575.
26. Q. Wei, S. Cheng, K.T. Ramesh, E. Ma, *Mat. Sci. Eng. A,* 381 (2004) 71.
27. F.H. Dalla Torre, R. Lapovok, J. Sandlin, P.F. Thomson, C.H.J. Davies, E.V. Pereloma, *Acta Mater.,* 52 (2004) 4819.
28. S. Li, I.J. Beyerlein, *Mod. Sim. Mat. Sci. Eng.,* 13 (2005) 509.
29. W.H. Huang, C.Y. Yu, P.W. Kao, C.P. Chang, *Mat. Sci. Eng. A,* 366 (2004) 221.
30. F.H. Dalla Torre, A.A. Gazder, E.V. Pereloma, C.H.J. Davies, *J. Mat. Sci.,* 42 (2007) 1622.
31. D.A. Hughes, N. Hansen, *Acta Mater.,* 45 (1997) 3871.
32. D.A. Hughes, N. Hansen, *Acta Mater.,* 48 (2000) 2985.
33. J.R. Bowen, *The Formation of Ultra-fine Grained Model Aluminium and Steel Alloys*, PhD. Thesis, University of Manchester Institute of Science and Technology, United Kingdom (2000).
34. G. Gottstein, L.S. Shvindlerman, *Grain Boundary Migration in Metals: Thermodynamics, Kinetics, Applications*, CRC Press, (1999), p. 408.
35. C.X. Huang, K. Wang, S.D. Wu, Z.F. Zhang, G.Y. Li, S.X. Li, *Acta Mater.*, 54 (2006) 655.
36. X.Z. Liao, Y.H. Zhao, S.G. Srinivasan, Y.T. Zhu, R. Z. Valiev, D. V. Gunderov, *App. Phys. Let.,* 84 (2004) 592.
37. X.Z. Liao, Y.H. Zhao, Y. T. Zhu, R.Z. Valiev, D.V. Gunderov, *J. App. Phys.* 96 (2004) 636.
38. J.W. Christian, S. Mahajan, *Prog. Mat. Sci.,* 39 (1995) 1.
39. E. El-Danaf, S.R. Kalidindi, R.D. Doherty, *Metall. Mat. Trans. A,* 30 (1999) 1223.
40. M.A. Meyers, L.E. Murr, *Acta Metall.,* 26 (1978) 951.
41. F.H. Dalla Torre, E.V. Pereloma, C.H.J. Davies, *Acta Mater.,* 54 (2006) 1135.
42. F.H. Dalla Torre, R. Lapovok, P.F. Thomson, J. Sandlin, C.H.J. Davies, E.V. Pereloma, *Materials Research Society Symposium*, USA (2004), p. 9.10.
43. V. Randle, *Acta Mater.* 52 (2004) 4067.
44. A.P. Sutton, R.W. Balluffi, *Interfaces in Crystalline Materials*, Clarendon Press, London (1997), p. 305.
45. S.D. Terhune, D.L. Swisher, K. Oh-Ishi, Z. Horita, T.G. Langdon, T.R. McNelley, *Metall. Mat. Trans. A,* 33 (2002) 2173.
46. S. Li, I.J. Beyerlein, M.A. Bourke, *Mat. Sci. Eng. A,* 394 (2005) 66.
47. J. Baczynski, *Torsion Textures Produced by Deformation and by Dynamic Recrystallisation in a-Iron and Two IF-Steels*, PhD. Thesis, McGill University, Canada (1996).
48. J. Baczynski, J. J. Jonas, *Acta Mater,,* 44 (1996) 4273.
49. F. Montheillet, M. Cohen, J.J. Jonas, *Acta Mater.* 32 (1984) 2077.
50. S. Li, I.J. Beyerlein, D.J. Alexander, S.C. Vogel, *Acta Mater.*, 53 (2005) 2111.
51. J. Markmann, P. Bunzel, H. Rösner, K. W. Liu, K. A. Padmanabhan, R. Birringer, H. Gleiter, J. Weissmüller, *Scr. Mater.,* 49 (2003) 637.
52. R.Z. Valiev, T.G. Langdon, *Prog. Mat. Sci.,* 51 (2006) 881.
53. M. Furukawa, Z. Horita, M. Nemoto, R.Z. Valiev, T.G. Langdon, *Mat. Char.* 37 (1996) 277.
54. K. Nakashima, Z. Horita, M. Nemoto, T.G. Langdon, *Acta Mater.* 46 (1998) 1589.
55. B.Q. Han, E.J. Lavernia, F.A. Mohamed, *Metall. Mat. Trans. A,* 34 (2003) 71.
56. M. Suś-Ryszkowska, T. Wejrzanowski, Z. Pakieła, K. J. Kurzydłowski, *Mat. Sci. Eng. A,* 369 (2004) 151.
57. B.Q. Han, E.J. Lavernia, F.A. Mohamed, *Metall. Mat. Trans. A,* 35 (2004) 1343.
58. J.E. Carsley, A. Fisher, W.W. Milligan, E.C. Aifantis, *Metall. Mat. Trans. A,* 29 (1998) 2261.
59. A.A. Gazder, E.V. Pereloma, C.H.J. Davies, *Mat. Sci. Eng. A,* 497 (2008) 341.
60. D. Kuhlmann-Wilsdorf, *Workhardening*, Gordon & Breach, New York (1968), p. 97.
61. D.L. Holt, *J. App. Phys.* 41 (1970) 3197.
62. F.H. Dalla Torre, E.V. Pereloma, C.H.J. Davies, *Scr. Mater.*, 51 (2004) 367.
63. K. Rhee, *Optimisation of the Thermo-Mechanical Treatment for Enhanced Formability of AA6111 Alloy Sheet*, PhD. Thesis, Monash University, Australia (2006).
64. J. Gil Sevillano, P. Van Houtte, E. Aernoudt, *Prog. Mat. Sci.* 25 (1981) 69.
65. E. Nes, *Prog. Mat. Sci.,* 41 (1997) 129.
66. U.F. Kocks, H. Mecking, *Prog. Mat. Sci.* 48 (2003) 171.
67. M. Zehetbauer, V. Seumer, *Acta Metall. et Mater.* 41 (1993) 577.
68. X.F. Fang, W. Dahl, *Mat. Sci. Eng. A* 203 (1995) 36.
69. X.F. Fang, C.O. Gusek, W. Dahl, *Mat. Sci. Eng. A,* 203 (1995) 26.
70. A.A. Gazder, S. Li, F.H. Dalla Torre, I.J. Beyerlein, C.F. Gu, C.H.J. Davies, E.V. Pereloma, *Mat. Sci. Eng. A,* 437 (2006) 259.